

This is the accepted version of the following article

Roman Svoboda, Jana Romanová, Stanislav Šlang, Iva Obadalová, Alena Komersová (2020). Influence of particle size and manufacturing conditions on the recrystallization of amorphous Enzalutamide. *European Journal of Pharmaceutical Sciences*. DOI: 10.1016/j.ejps.2020.105468

This accepted version is available from URI <https://hdl.handle.net/10195/77084>

Publisher's version is available from:

<https://www.sciencedirect.com/science/article/pii/S0928098720302578?via%3Dihub>



This version is licenced under a [Creative Commons Attribution-NonCommercial-NoDerivatives 4.0 International](https://creativecommons.org/licenses/by-nc-nd/4.0/).

Influence of particle size and manufacturing conditions on the recrystallization of amorphous Enzalutamide

Roman Svoboda^{*1}, Jana Romanová¹, Stanislav Šlang², Iva Obadalová³, Alena Komersová¹

¹*Department of Physical Chemistry, Faculty of Chemical Technology, University of Pardubice, Studentská 573, 532 10 Pardubice, Czech Republic.*

²*Center of Materials and Nanotechnologies, Faculty of Chemical Technology, University of Pardubice, Studentská 573, 532 10 Pardubice, Czech Republic.*

³*Zentiva, k.s., U Kabelovny 130, Prague 10, Czech Republic*

Abstract

Non-isothermal differential scanning calorimetry was used to study the influences of particle size and mechanically induced defects on the recrystallization kinetics of amorphous Enzalutamide. Enzalutamide prepared by hot melt extrusion and spray-drying was used as a model material. The recrystallization rate was primarily accelerated by the presence of the processing-damaged surface of the powder particles. The actual surface/volume ratio associated with decreasing particle size fulfilled only a secondary role. Interestingly, higher quench rate during the extrusion led to a formation of thermally less stable material (with the worse stability being manifested via lower activation energy of crystal growth in the amorphous matrix). This can be the consequence of the formation of looser structure more prone to rearrangements. The recrystallization kinetics of the prepared Enzalutamide amorphous materials was described by the two-parameter autocatalytic kinetic model. The modified single-curve multivariate kinetic analysis (optimized for the data obtained at heating rate $0.5\text{ °C}\cdot\text{min}^{-1}$) was used to calculate the extrapolated kinetic predictions of long-term isothermal crystal growth. The predictions were made for the temperatures from the range of drug shelf-life and processing for each particle size fraction. By the combination of the mass-weighted predictions for the individual powder fractions it was possible to obtain a very

* Corresponding author: Tel.: +420 466 037 346 E-mail address: roman.svoboda@upce.cz

reasonable (temperature-extrapolated) prediction of the crystallization rate for the as-prepared unsieved powdered amorphous Enzalutamide.

Keywords: amorphous drug; Enzalutamide; recrystallization; prediction; particle size

1. Introduction

Enzalutamide is one of the recently developed androgen receptor antagonist for the treatment of castration-resistant prostate cancer (CRPC) (Chen et al., 2004; Tran et al., 2009; Jung et al., 2010). This new nonsteroidal antiandrogen shows significantly higher affinity (~ 10 times) to the androgen receptors and exhibits a very favorable toxicity profile (C. Tran et al., 2009). This makes Enzalutamide a promising substitute for the former generation of CRPC drugs (currently available as XTANDI (Roseler, 2015)). In order to increase the aqueous solubility and bio-availability (Rams-Baron et al., 2018), the API (active pharmaceutical ingredient) is being considered for utilization in its amorphous form. For the majority of nowadays developed APIs, the biopharmaceutical properties such as e.g. dissolution characteristics, stability in the physiological fluids, permeability and metabolism by gastrointestinal enzymes are highly crucial (Jung et al., 2010; Jemal et al., 2006; Tyrrel, 1998; Chen et al., 2004; Tran et al., 2009). One of the most common approaches to enhance the dissolution characteristics is the conversion of the API into amorphous/glassy form (Schittny et al., 2020). However, the amorphous state is not associated only with benefits - e.g. the faster dissolution rates (Jung et al., 2010; Zhou et al., 2003) or approx. 10 - 1500x higher water-solubility (Hancock and Zografi, 1997) due to the lower intermolecular forces compared with their crystalline counter parts). It comes also with a major flaw – the lower thermal stability – which unfavorably influences the drug shelf-life and processing options. Note that the dissolution rates of solid dispersions of amorphous and crystallized

Enzalutamide in hydroxypropyl methylcellulose and copovidone were recently tested in vitro and in vivo (Wilson et al., 2018).

In the past decades, a lot of active research took place with regard to the amorphous pharmaceutical solids and their stability against recrystallization, including both the crystal growth above and below the glass transition temperature (T_g) (Yu, 2001; Bhugra and Pikal, 2008; Janssens and den Mooter, 2009; Bhattacharya and Suryanarayanan, 2009; Sun et al., 2012). A considerable number of the recrystallization studies is nowadays being performed by using the non-isothermal differential scanning calorimetry (DSC). But only recently, see (Romanová et al., 2018), very few satisfactory predictions towards the below- T_g crystal growth could be made based on the DSC data. It was shown in that paper (the study was performed for Enzalutamide) that by considering the temperature-based evolution of the above- T_g non-isothermal recrystallization kinetics a correct prediction of the degree of amorphous-to-crystalline conversion can be made for the temperatures (storage) below the glass transition temperature. Due to the simplicity and rapidity of the DSC measurements, the approach presented in this paper appears to be a very promising route for complementing/replacing the time-consuming stability tests (Laitinen et al., 2013).

The present study will continue the research presented in (Romanová et al., 2018), exploring the influence of different preparation routes (hot melt extrusion to different temperatures + spray drying) on the thermal stability and crystal growth processes in the amorphous Enzalutamide. The study aims to quantify the influence of particle size, storage temperature and storage conditions on the recrystallization kinetics. We also plan to develop the corresponding methodologies to appropriately account for these influences. The investigated particle size distribution will cover the usual range found in pharmaceutical applications.

2. Experimental

Three batches of amorphous Enzalutamide were prepared from the crystalline R1 polymorphic form (Zentiva Group, k.s., Czech Republic). The first two batches were produced by the hot-melt double-screw extruder HME (Three-Tec, GmbH, Seon, Switzerland), with conditions set to approx. 230 °C and 100 rpm. The first batch of the amorphous material was produced in the standard way, when the molten material solidified at the laboratory temperature. Preparation of the second batch utilized a heat sink (aluminum desk) cooled to the temperature of liquid N₂. In both cases, macroscopic droplets of glassy Enzalutamide were formed. These were consequently shortly ground in a ball mill (MM200, Retsch; 10 Hz, 30 s, ZrO₂ balls, dry) and then sieved through sieves (Retsch; tapping with no pressure) with defined mesh size. The following powder size fractions were prepared: 20 – 50, 50 – 125 and 300 - 500 µm (note that the 300 - 500 µm particle size is not realistically utilizable in the pharmaceutical applications and its experimental use in this study was to help the development of the crystallization models and comparisons). The third batch of amorphous Enzalutamide was prepared by spray drying in the Büchi Mini Spray Dryer B-290 (inlet 85 °C, aspirator 100 %, pump 20 %, nozzle cleaner 2) → 25 grams were dissolved in 500 ml of methanol (p.a.), the yield was approx. 75 %, the material was dried in a vacuum dryer at 40 °C for 100 hours. During this time (~ 100 h), the HME-produced materials were stored at 10 °C in a desiccator. After this time, the characterization of the materials and the kinetic measurements were performed. At this stage, thermogravimetry (TGA 4000, Perkin Elmer) measurements were performed at 10 °C·min⁻¹ in N₂ atmosphere, showing no significant contents of residual solvent (~ 0.08 w.% for spray-dried product) or water (~ 0.11 w.% for spray-dried product and 0.29 w.% for HME product). All volatiles were released below the onset of the crystallization process. Infrared spectroscopy (6700 FTIR Spectrometer, Nicolet) measurements were performed for the HME-produced and spray-dried

materials, confirming the similarity of the spectra and indicating (together with no detectable coloring) that HME did not result in the degradation of Enzalutamide.

The recrystallization kinetics was investigated by the Q2000 heat-flow differential scanning calorimeter DSC (TA Instruments, New Castle, USA) equipped with an autosampler, an RCS90 cooling accessory, and T-zero technology. The DSC was calibrated using In, Zn, and H₂O; dry N₂ was used as purge gas at a flow rate of 50 cm³·min⁻¹. Samples from each Enzalutamide batch/powder fraction were hermetically sealed in low-mass T-zero DSC pans (thus the measurements were effectively realized in air atmosphere). The average sample masses were ~ 2 mg. For each Enzalutamide batch/powder fraction a set of measurements was performed in the form of simple heating scans (always utilizing a fresh as-prepared sample) at heating rates $q^+ = 0.5, 1, 2, 5, 10$ and 20 °C·min⁻¹. The measurements were performed in the 5 – 220 °C temperature range. Very good repeatability was confirmed based on the several reproduced measurements.

The amorphous nature of the prepared Enzalutamide materials as well as the similar identity for the DSC-crystallized products were confirmed by a X'PERT PRO MPD PANalytical diffractometer equipped with X'Celerator detector (2 – 40° 2θ range, step 0.01°, 312 s per step, CuKα). The morphology of the as-prepared and DSC-crystallized samples was investigated using SEM microscope Lyra 3 (Tescan). The nuclear magnetic resonance spectra of the as-prepared samples were measured via NMR spectrometer Bruker Avance III 400 WB (¹⁹F MAS method – 2.5 μs pulses with 4 s delay and 400 repetitions, rotor size 2.5 mm, spinning rate 30 kHz).

3. Results

Thermokinetic profile of the three Enzalutamide batches was investigated by DSC in dependence on particle size. Example DSC curves obtained at 10 °C·min⁻¹ is shown in Fig.1

powdering. In the last case, by the defects we mean a simplifying denomination for amorphous regions with higher energy, such as micro-fractures, sharp edges, internal mechanical stresses, etc. – these will be for simplicity referred to as “defects” further on. The internal stresses should however influence the crystallization only slightly because majority of them should be removed above T_g . The surface area of the present milled products was not measured. However, it is obvious that the presence of mechanical defects increase the total surface area of the particles. A more detailed explanation regarding the correlation between the particle size and surface-to-volume ratio, and the estimates of the surface/volume ratios for the present Enzalutamide products can be found in the Supplemental online material.

The larger particles produced by crushing the HME product exhibit a single-peak behavior, where the crystallization onset shifts to lower temperatures with decreasing particle size ($125\text{ }^{\circ}\text{C} \rightarrow 120\text{ }^{\circ}\text{C}$). The lowest size HME-produced particles show a complex crystallization with the onset immediately following T_g . As is well known, crystallization of organic glasses starts from surface (which is also true for Enzalutamide, as will be demonstrated later). In our preceding work on Enzalutamide (Romanová et al., 2018) it was shown that the presence of mechanically induced defects (Svoboda and Brandová, 2017; Brandová et al., 2018) plays major role in the crystallization process. In case of the lowest size (20 - 50 μm) material, an excessive amount of mechanical defects and fractures apparently occurs on the surface of the particles. This apparently leads to the acceleration of the crystal growth process (as demonstrated by the early onset) and diversification of the crystals morphologies (as indicated by the reproducibly complex set of overlapping crystallization processes). The diversity of crystal morphologies was confirmed by SEM, as will be discussed later in this section. Also, the complex crystallization behavior indeed indicates the presence of multiple kinetic processes – origin and possible attribution of the kinetic peaks to the particular crystallization processes will be discussed in Section 4.1. The

spray-dried material has much smaller particle size (0.1 – 1 μm , compared to the 20 - 50 μm for HME) and thus much higher surface-to-bulk ratio (approx. two orders of magnitude higher compared to the 20 - 50 μm HME powder; see the Supplemental online material). However, the spray-dried material exhibits the crystallization (though complex) in the same temperature range as the coarse HME batches. This implies that it is indeed the mechanically induced defects produced by ball milling (sharp edges, micro-fractures, internal stresses, etc.) that are crucial for early initiation of the nucleation and crystal growth. These features are abundant in case of the mechanically crushed/milled powders but scarce for perfectly spherical particles produced during the spray drying. This indeed indicates that the crystallization of amorphous Enzalutamide is largely dominated by crystal growth from the mechanically activated crystallization centers as compared to the nuclei formed at the flat surfaces during the material preparation or (in correspondence with the classic nucleation theory) during the DSC heating experiment. Note that even though the spray-drying and extrusion are conceptually different preparation processes (bottom-up vs. top-down, respectively). However, considering the otherwise akin behavior (XRD, NMR, position of T_g , kinetic parameters, type of crystallization complexity) it is still safe to say that the influence of the different manufacturing conditions is much lower than the influence of the massive difference in the surface-to-volume ratios between the spray-dried product and 20 – 50 μm powder. In addition, one can also note the resembling crystallization complexity between the LN_2 -cooled 20 - 50 μm powder and spray-dried particles. This resemblance may correspond to the similar crystal morphologies occurring in these two cases. It is also noteworthy that, in addition to the ball-milling, similar particle size fractions were from the HME-produced Enzalutamide prepared also by grinding with agate mortar and pestle. The DSC, XRD and NMR measurements of these products were extremely similar to those reported for the ball milled products in the present study. This indicates that at least for the short milling periods the

amounts of mechanically induced defects and the approximate surface-to-volume ratios are quite similar for these two powdering techniques.

The amorphous character of the as-prepared materials was investigated via solid-state NMR. In Figs. 2A and 2B the NMR spectra of the present substances are shown in comparison with the arbitrarily prepared mixed “semi-crystalline” powders. The mixtures were prepared in weight ratios mentioned in Figs. 2A and 2B (1 and 5 w.%). The mixtures were prepared from the original R1 crystalline Enzalutamide material (used for the preparation of the amorphous batches) and the fully amorphous material as prepared previously (Romanová et al., 2018). Whereas the LN₂-cooled and spray-dried materials appear to be amorphous, the air-cooled batch of Enzalutamide seems to contain a low amount of crystals (well below 1 wt.%). This can be explained by the lower effective cooling rate being developed during the cooling in air (during slower cooling the nuclei had more time to grow and form nanocrystallites). Similar investigation was performed also by means of XRD – see Fig. 2C. As is apparent, the XRD technique is much less sensitive to the low (sub 1 wt.%) amounts of crystalline material, as all three Enzalutamide batches appear to be fully amorphous compared to the mixed “semi-crystalline” powders. Note that the tests were performed for the powdered materials in order to check the possible degradation of the amorphous matrix due to the ball milling procedure - see e.g. (Trasi et al., 2010) where crystallization behavior of griseofulvin was influenced by the milling process. In the present case, however, the transfer of mechanical energy did not have impact on the amorphous character of the powdered product as can be derived from the comparison of the air-cooled and LN₂-cooled NMR spectra shown in Fig. 2A. The X-ray diffraction was also used to characterize the DSC-crystallized products and to confirm that all three batches of amorphous Enzalutamide crystallize into the R1 polymorphic form that was originally used for their preparation – see Fig. 2C. The question of the possible polymorphic transitions was (apart

from the XRD analyses performed with respect to all main crystallization peaks) ruled out also based on the uniformity of the observed melting peaks onsets. For more information on Enzalutamide polymorphs see e.g. (Maini et al., 2018).

Important insight into the crystal growth processes was provided by the scanning electron microscopy of partially and fully crystallized samples. In Fig. 3 the SEM micrographs of the air-cooled and LN₂-cooled HME-produced 20 - 50 µm powders are shown. In the case of the partially crystallized samples (micrographs A and C), the surface of the powder particles looks relatively similar, with the crystallites in the form of lumps, nuggets and scales. It is also clear that all crystal growth proceeds from surface. On the other hand, the fully crystallized samples of the lowest size powders prepared from HME-produced Enzalutamide (micrographs B and D) show marked differences. Whereas the surface of the LN₂-cooled material looks more-or-less similar to that of partially crystallized powders, advanced crystallization of the air-cooled material leads to formation of outwards growing needles, plates and fibers. The dissimilar morphology of secondary crystallites well corresponds to the marked difference between the shapes of the DSC crystallization signals – this will be further commented in section 4.1.

In contrast with the low sized powders, the coarse Enzalutamide particles (300 - 500 µm) crystallize uniformly regardless of the applied cooling rate during the extrusion (i.e. air-cooled vs. LN₂-cooled). A representative depiction of the surface and cross-section of the partially crystallized HME-produced material is shown in Fig. 4A. Similar cross-sections (finely structured surface crystallites growing inwards) and surfaces (relatively smooth with no outwards-growing formations) were obtained for the air-cooled and LN₂-cooled partially crystallized coarse powders (the same was valid also for fully crystallized coarse powders). In Fig. 4B the detailed view of the lamellar structure of the surface crystals is shown. Very rarely, grain-like volume-located crystallites could be found on the cross-section micrographs

of the LN₂-cooled partially crystallized coarse powders (see Fig. 4C). These crystallites acted as the crystallization centers for the secondary growth of rod/fiber-like crystals on the newly formed (after the fracture of the powder particle) surface. These volume-located crystallite formations were found specifically in off-broken edges and tips of the large particles, which would indicate the volume crystallization accelerating effect of the internal micro-fractures and stresses from fast cooling. However, in that case a similar manifestation would be expected also for the finely powdered Enzalutamide. Alternative explanation may be that the volume-located crystallites (or the crystallization centers responsible for their growth) originate from the extrusion process itself with the particle coming from the original surface of the HME-processed bulk material. In such case the finely powdered particles would probably form by chipping off along these micro-cracks, creating a new surface instead of the volume-located micro-crack. Nonetheless, the scarcity of the volume-located crystalline structures allows for their neglecting in any evaluations presented in the current paper. Last micrograph, shown in Fig. 4D, depicts the partially crystalline spray-dried (SD) particle. Again, the typical scale-like shape of the surface crystallites can be seen.

Correlation between the SEM micrographs and the DSC curves can be found in the Supplemental online material. Also, for comparison, the SEM micrographs of amorphous HME-produced and spray-dried samples are shown in the Supplemental online material.

4. Discussion

4.1. Kinetic description

In the present section the influence of the particle size on recrystallization behavior of the amorphous APIs will be demonstrated by means of the standard kinetic analysis. The DSC data obtained for the two HME-processed Enzalutamide batches at different heating rates q^+ are shown in Fig. 5. As was already mentioned above, the crystallization behavior (and the

associated shape of the DSC curves) drastically changes with applied q^+ . In case of the coarse powders, the decreasing q^+ leads to prolonged crystallization onset tail and the sharply decreasing high-T side of the crystallization peak. These are the typical zero-order kinetics features characteristic for crystallization of organic glasses (Rams-Baron et al., 2018; Qin and Ting, 2017; Dobрева et al., 1996) (growth originating strictly from surface, employing high number of crystallization centers). Note that at high q^+ the crystallization peaks resemble the so-called nucleation-growth kinetic behavior (exhibiting characteristic negative asymmetry of the DSC peak with round top). This resemblance is however most probably the consequence of thermal gradients resulting in surplus energy favoring certain crystallization centers (as opposed to the manifestation of the true nucleation-growth JMA kinetics, where either surface- or volume-located nuclei formed in accordance with the classic nucleation theory grow at constant rate while forming symmetric rod-, plate- or sphere-like objects). In case of the the lowest size powders (both air- and LN₂-cooled), the crystallization behavior is complex, manifesting multiple kinetic peaks. The first crystallization peak has the typical Johnson-Mehl-Avrami (Johnson and Mehl, 1939; Avrami, 1939; Avrami, 1940; Avrami, 1941) (nucleation-growth JMA) behavior. This indicates that the highly damaged surface results in preferred crystal growth from the mechanically induced defects that mimic the nucleation effect from the JMA model. It is also very important to note that the decreasing q^+ leads in case of the 20 - 50 μm powders to the increased separation of the first crystallization peak. The separation happens due to the difference in activation energies of the involved sub-processes, as will be discussed later. This will be crucial for the consequent extrapolation/prediction of the kinetic behavior to lower (storage or processing) temperatures. Furthermore, the second crystallization process that is very pronounced in case of the air-cooled HME material appears to be associated with the surface formation of the outwards growing needles, plates and fibers as evidenced by SEM microscopy. Regarding the third

crystallization peak, we assume that it may be associated with the secondary crystallization (originating at the volume located crystal/glass interfaces) that fills the gaps in-between the crystallites formed from the defects (first crystallization peak).

In order to quantify the manifestation of the crystallization processes, the kinetic analysis of the DSC data can be used. The kinetic analysis is based on enumerating the basic kinetic equation (Šesták, 1984), derived to describe the DSC signal:

$$\Phi = \Delta H \cdot A \cdot e^{-E/RT} \cdot f(\alpha) \quad (1)$$

where Φ is the measured heat flow, ΔH is the crystallization enthalpy, A is the pre-exponential factor, E is the apparent activation energy of the crystallization, R is the universal gas constant, T is temperature and $f(\alpha)$ stands for an expression of a kinetic model with α being conversion. The standard methodologies utilized for the kinetic calculations are then e.g. the Kissinger (Kissinger, 1957) (Eq. 2) or Starink (Starink, 2003) (Eq. 3) methods for the determination of E , and the characteristic kinetic functions (Svoboda and Málek, 2011) or the multivariate kinetic analysis MKA (Opfermann, 2000) (Eqs. 4 and 5) for the determination of the $f(\alpha)$ model function:

$$\ln\left(\frac{q^+}{T_p^2}\right) = -\frac{E}{RT_p} + const. \quad (2)$$

$$\ln\left(\frac{q^+}{T_\alpha^{1.92}}\right) = -1.0008 \frac{E}{RT_\alpha} + const. \quad (3)$$

$$RSS = \sum_{j=1}^n \sum_{k=First_j}^{Last_j} w_{j,k} (Y_{exp_{j,k}} - Y_{cal_{j,k}})^2 \quad (4)$$

$$w_j = \frac{1}{\left[\left[\frac{d\alpha}{dt} \right]_{\max} \right]_j + \left[\left[\frac{d\alpha}{dt} \right]_{\min} \right]_j} \quad (5)$$

where T_p is the temperature corresponding to the maximum of the crystallization peak, T_α and E_α are the temperature and activation energy corresponding to certain chosen values of conversion α , RSS is the sum of squared residue, n is number of measurements, j is index of

the given measurement, $First_j$ is the index of the first point of the given curve, $Last_j$ is the index of the last point of the given curve, $Y_{exp,j,k}$ is the experimental value of the point k of curve j , $Y_{cal,j,k}$ is the calculated value of the point k of curve j and w_j is weighting factor for curve j . The standard model functions $f(\alpha)$ utilized for the crystallization processes then include the nucleation-growth JMA (Eq. 6) and the autocatalytic AC (Šesták, 1984) (Eq. 7) models:

$$f(\alpha) = n(1 - \alpha)[- \ln(1 - \alpha)]^{1-(1/n)} \quad (6)$$

$$f(\alpha) = \alpha^M (1 - \alpha)^N \quad (7)$$

where n , M and N are the kinetic exponents of the given models.

The results from these evaluation procedures are usually presented in their mean form. This is demonstrated for the present data in Figs. 6A - 6C and Table 1A, where the results of kinetic analysis (averaged for all applied q^+) are shown in dependence on particle size d_{aver} . As can be seen, these results exhibit relatively large errors due to the variability of the kinetics with applied q^+ . Exemplary demonstration of these trends arises in the case of the crystallization enthalpy (see Fig. 6A), where the error bars for the overall ΔH for the 20 - 50 μm powders reach almost 40 % of the nominal value. Whereas this is a rather extreme example, the systematic q^+ -related errors associated with the other determined quantities and particle sizes are still significant – the Student's t-test was used to confirm the statistical significance of the trends displayed in Figs. 6A - C.

Nonetheless, even the averaged results still provide some meaningful information. The average crystallization enthalpy is $\sim 55 \text{ J}\cdot\text{g}^{-1}$, not significantly changing with particle size in the high d_{aver} region with the exception of the lowest size powder materials that exhibit significantly lower $\Delta H \approx 40 - 45 \text{ J}\cdot\text{g}^{-1}$. Note that this is rather a consequence of the high surface-to-volume ratio compared to the presence of mechanically induced defects. The SD-produced Enzalutamide exhibits lowest ΔH despite having minimum processing-related

defects. The first crystallization process occurring for the 20 - 50 μm powders, decisive for the crystallization tendency, accounts for approx. 20 – 30 % of the overall finest powder size ΔH . Note that the crystallization enthalpies indeed correspond to the fully crystalline materials. We have checked this by performing additional cooling and re-heating steps following the formation of the crystallization peak (i.e. before the temperature of melting was reached). No additional crystallization was observed during the cooling step. No T_g effect or crystallization peak were observed during the second heating scan. Examples of these measurements are included in the Supplemental online material.

The so-called Kissinger plot (Fig. 6B) depicting the dependence of T_p on q^+ shows the marked accelerating effect of mechanically induced defects (mostly present for the 20 - 50 μm powders) on the crystallization process. Again, note that the SD-produced material with largely smaller particles (mostly in the range 0.1 – 2 μm) crystallizes at significantly higher temperatures compared to the 20 - 50 μm powders, where the surface of particles is however significantly corrupt. The crystallization complexity of the spray-dried Enzalutamide is also manifested by switching between the major intensities of the dominant growth sub-processes – see the two deviated points obtained at highest q^+ . In addition, also a systematic difference between the T_p values of air-cooled and LN_2 -cooled products is apparent (and statistically significant), with the air-cooled materials achieving the maximum crystallization rate slightly earlier (at lower temperature). This is the consequence of the larger number of nuclei being formed during the slower HME cooling. It is noteworthy that the material thermal conductivity and thermal gradients can affect the kinetics calculated from the DSC measurements. With regard to the particle size it is generally the low sized powders (that have large amount of air gaps if multilayered in the DSC pan) that are prone to the influence by the overall systematic thermal conductivity. On the other hand, the larger particles can suffer from the delayed heat transfer with the particles themselves. However, the presence of

thermal gradients is characterized (Svoboda et al., 2020) by a significant curvature of the Kissinger plot, which is not observed for any Enzalutamide product shown in Fig. 6B. In addition, the experimental conditions (low sample masses, low-to-moderate q^+ , samples carefully spread on the bottom of the DSC pans) ensured minimization of the possible influence of the systematic thermal lags.

The most important information from the standard preliminary (overall) kinetic analysis is that about the apparent activation energy E – see Fig. 6C. The depicted data are those determined by the iso-conversional Starink method (that calculates and averages E over the entire course of α). All values were in a good agreement with the results of the (slightly less precise) Kissinger method. In case of the 20 - 50 μm powders, the graph shows only results for the first crystallization peak. This peak is in the present case (lowest E out of all involved sub-processes; see Figs. 5A and 5B for the increased peak separation with decreasing q^+) paramount for the crystallization tendency and thermal stability of the material. The significantly higher E ($\sim 190 \text{ kJ}\cdot\text{mol}^{-1}$) of the SD-produced Enzalutamide indicates, together with the crystallization already manifesting at higher temperatures, a better thermal stability compared to the lowest size HME product. Note that the thermal stability of the glasses is from the kinetic point of view driven by the model-free parameters: E and A . Whereas the pre-exponential factor A can be perceived as responsible for the actually measured position of the crystallization peak (and as such determines the stability of the glass with respect to the measured temperature range), the activation energy dictates the stability of the glass extrapolated to lower temperatures. I.e. for practical purposes the crystallization onset measured at high temperatures (= high heating rates) is almost irrelevant. The major factor is the magnitude of E , which determines the pace at which the onset will shift to lower temperatures with lowering q^+ (in general the glasses with higher E tend to be significantly more stable).

It is also noteworthy that the stability of the glass is related to the amount of nuclei/crystallites formed during the cooling process. Here the common sense would dictate that at slower cooling more nuclei form and the consequent crystallization is faster. However, when nucleation proceeds very slowly, the actual crystal growth apparently dominates with regard to the value of activation energy (see Fig. 6C). This is indeed the case of Enzalutamide, where very few crystals form at the surface of a heated bulk material, i.e. low number of nuclei forms, as was evidenced by optical microscopy. Also, the looser structure of the LN₂-cooled glassy matrix together with the possible higher stress within the sample allow the accelerated crystallization.

4.2. Kinetic predictions

In the previous section the standard methodological approach utilized in the kinetic analysis was adopted to show the influence of powder particle size on crystallization behavior of amorphous Enzalutamide. Nonetheless, the high-temperature (non-isothermal) crystallization data are usually of limited use in practice. The main purpose of kinetic analysis is to provide the possibility of kinetic predictions extrapolated towards the lower (around or sub T_g) temperatures, where storage and processing of the amorphous materials takes place. As was reported in our previous paper (Romanová et al., 2018), the accuracy of such predictions depends crucially on the correct selection of kinetic parameters used for the simulation. The data from the lowest q^+ (behavior closest to the isothermal state $q^+ = 0 \text{ } ^\circ\text{C}\cdot\text{min}^{-1}$) have to be used, and high descriptive accuracy of the onset edge of the DSC peak has to be prioritized. This can in practice be done by adjusting the weighting w_j from Eq. 5 to a lower value for data on the high- α side of the kinetic peak. The algorithm utilizes the maximum da/dt as the breakpoint. We recommend the w_j values of 1 and 0.3 to be used for the low- α and high- α data, respectively). In case of this “prediction-optimized” approach,

very good predictions can be made even for temperatures more than 50 °C below the experimentally measured ones (as was shown in (Romanová et al., 2018)).

In Figs. 7A – 7D such predictions are depicted for the present measurements that were carried out in dependence on particle size. In compliance with (J. Romanová et al., 2018), the kinetic parameters determined via the modified single-curve MKA (Romanová et al., 2018; Brandová et al., 2018; Svoboda et al., 2018) for the DSC data obtained at 0.5 °C·min⁻¹ were used for the simulations. The parameters are listed in Table 1B. In case of the 20 - 50 µm powders the simulations are based only on the kinetic parameters corresponding to the first DSC peak. With the distribution of activation energies found for the finest powders of both HME-produced materials it is only the first sub-process that determines the thermal stability of the amorphous matrix. Clearly, all particle size fractions of the amorphous Enzalutamide exhibit a significantly manifesting temperature-dependent kinetic behavior. This is indicated by the large differences between the mean (Table 1A) and “prediction-optimized” (Table 1B) parameters values. The differences also stress the importance of utilizing the advanced kinetic approach. Especially the model-free parameters (E and A) are crucial and their change by the amount similar to that between Tables 1A and 1B can result in several orders of magnitude large deviations in predicted crystalline content α .

The predictions presented in Figs. 7A – 7D also demonstrate the huge effect of particle size and presence/absence of the mechanically induced defects on the thermal stability and shelf-life of amorphous pharmaceutical ingredients. It should be borne in mind that the several orders of magnitude large differences in crystallization rate are the consequence of the non-isothermally measured crystallization peak being shifted by only ~ 20 – 30 °C (see Figs. 1 and 5). Apart from the markedly accelerating influence of the mechanically induced defects on the crystal growth rate, the isothermal predictions calculated from the low- q^+ data also confirm several other previous findings based on the non-isothermal measurements. The

kinetic crystallization rate $d\alpha/dt$ (as opposed to ΔH) is primarily driven by the presence of mechanically activated regions and not by d_{aver} . The SD-produced Enzalutamide is significantly more stable compared to the lowest size HME powders. Interestingly, the N_2 -cooled HME material is significantly less thermally stable than the air-cooled one. This is despite the NMR data showing a minor infusion of crystallinity in the initially prepared air-cooled material (see Figs. 2A and 2B), and the high- q^+ non-isothermal DSC data indicating the opposite trend in stability (see Fig. 1). One possible explanation may have to do with the occasional presence of the inside-located crystallites found for the coarse powder particles of the N_2 -cooled HME (see Fig. 4C), where the same conditions allowing the formation of such crystallites would certainly accelerate the overall crystallization process.

The crystallization kinetics depends significantly on the particle size. Therefore, we wanted to explore the possibility of the combined kinetic predictions (such as those depicted in Figs. 7A – D) weighted by the actual representation of the particular powder fraction being able to describe the crystallization signal for the as-prepared powdered (unsieved) amorphous Enzalutamide. We have tested this for the air-cooled HME material, for which we have obtained the particle size distribution (defined via the weight percentage of the sieved powder fractions) shown in red in Fig. 7E. Crystallization of the sample taken from the unsieved material was measured in DSC isothermally at 100°C . See the black curve in Fig. 7F for the α -t dependence and the inset for the raw heat flow signal. In the first approximation we have used only the three predictions (black curves in Fig. 7C) provided for the three air-cooled HME particle size fractions studied in the present paper (20 - 50 μm , 50 - 125 μm , 300 - 500 μm). We did this to fit (using non-linear optimization) the experimental α -t data with the weighing factors being variable:

$$\alpha_{\text{exp}} = \sum w_i \cdot \alpha_{pi} \quad (8a)$$

$$\sum w_i = 1 \quad (8b)$$

where α_{exp} represents the experimentally obtained data, α_{pi} are the individual theoretical predictions for the given d_{aver} , and w_i are the corresponding weighting factors. The result of the best fit is represented by the red dashed line in Fig. 7F.

In order to account for the missing powder fractions we have, in the second approximation, added predictions for the following particle size fractions typically prepared in our lab: 125 – 180, 180 – 250 and 250 - 300 μm . The predictions were derived/calculated via arbitrary interpolation of the kinetic parameters obtained for the two boundary fractions (50 – 125 and 300 – 500 μm):

$$P_i = \frac{k_i}{4} \cdot (P_{300-500} - P_{50-125}) + P_{50-125} \quad (9)$$

where P_i is the value of kinetic parameter (E, A, M or N) for i th powder size fraction, $P_{300-500}$ and P_{50-125} are the values of that parameter for the indexed fractions, and k_i is 1, 2 and 3 for the 125 – 180, 180 – 250 and 250 - 300 μm fractions. In this way, a series of gradually slowed down crystallization processes was implemented into the non-linear optimization in the 50 – 500 μm d_{aver} range. The corresponding fit of the experimental data is shown by the blue line in Fig. 7F. The determined weighting factors w_i (variables from Eq. 8 that should represent the participation of the particular powder fractions) are expressed as weight percent by the blue columns in Fig. 7E. As can be seen, the largest deviations from the true representation of the powder fractions (determined via the comparison of the red and blue columns in Fig. 7E) were found for the lower sized fractions 20 – 50, 50 – 125 and 125 - 180 μm . Three things should be borne in mind when explaining this discrepancy. Firstly, the largest deviations in Fig. 7E correspond to the α range with worst descriptive correlation in Fig. 7F, thus the calculated weight distribution does not necessarily need to correspond to the reality. Secondly, the powder fraction weight distribution in the measured sample did not have to be representative of the whole batch. Thirdly, from the mathematical point of view, the main problem of the optimization was the concave experimental data being fit by the convex

predictions. Note that the convex shapes of the modeled curves undisputedly result directly from the raw experimental data depicted in Fig. 5.

If we force the w_i values corresponding to the true overall powder size distribution into the optimization procedure, it is indeed apparent that the main problem is the convex predictions of the 50 – 125 and 125 - 180 μm fractions (that account for the largest discrepancy in the 10 – 70 % α range) describing the convex-shaped experimental data. In other words, the accelerating kinetic model $f(\alpha)$ predicted from the non-isothermal measurements in case of these powder fractions appears to not agree with the decelerating crystallization at 100 °C. However, the accelerating quasi-zero-order model occurs unambiguously for these particle size fractions below 120 °C (see Fig. 5C). One of the possible explanations is that the particle size range of the 50 - 125 μm powder fraction is too large to properly account for the transition between the two types of crystallization behavior observed for the 20 - 50 and 50 - 125 μm fractions. Also, the split of the 50 - 125 μm d_{aver} range would lead to a significantly better description as in the case of the transition from 50 - 125 μm to 300 - 500 μm . I.e. the procedure applied in the second approximation, as described above, where the concave curve can be modeled via larger number of small convex contributions. Alternatively, it can be an external influence that is responsible for the increased rate of crystallization. In particular, the presence of the finest powder fraction 20 - 50 μm that very quickly crystallizes below 100 °C may speed up the crystallization of the larger amorphous particles. This effect could proceed either by locally increasing the temperature (crystal growth is exothermic) or by some effects similar to seeding in solutions. Exact nature of this potential process remains to be solved. Nonetheless, it was shown that the combination of the kinetic predictions from non-isothermal measurements of particular particle size fractions can very reasonably describe the isothermal crystallization of the initial unsieved material extrapolated to lower temperatures.

4. Conclusions

The influences of particle size and mechanically induced defects on the crystallization behavior of amorphous Enzalutamide were demonstrated via non-isothermal DSC experiments. Series of the thermo-kinetic measurements were performed at different q^+ for the 20 – 50, 50 – 125 and 300 – 500 μm particle size fractions of hot-melt-extruded material, and for the spray-dried material. Presence of mechanically induced defects was found to dominantly accelerate the crystallization. The pure surface-to-volume ratio (i.e. intensity of crystal growth initiated from flat surfaces) had less pronounced effect in comparison to the growth from mechanically activated centers. This was indicated by the data for spray-dried material. The higher quench rate during the amorphization resulted in the significantly lower thermal stability of coarser powder fractions. This effect was manifested through the lower apparent activation energy of the crystal growth, which means that its importance increases with the extrapolation to lower temperatures. The influence would possibly be comparable to that of the mechanically induced defects at laboratory temperatures.

In addition, the observed crystallization kinetics was for all studied materials described by the autocatalytic AC model. By using the modified single-curve multivariate kinetic analysis (optimized for the measurements at $0.5\text{ }^\circ\text{C}\cdot\text{min}^{-1}$) the predictions of crystal growth rate kinetics were calculated for long-term isothermal annealings (akin to the processing and shelf-life thermal histories). A reasonable prediction of the extrapolated isothermal crystallization kinetics of unsieved powdered material was obtained by combining the kinetic predictions for the particular powder fractions obtained non-isothermally. The possible explanations for the higher-than-predicted initial crystallization rate involve the seeding effect of quickly crystallizing fine particles and the neglected transition between the significantly differing kinetics of the 20 – 50 and 50 – 125 μm powder fractions.

To conclude, the presence of mechanical defects plays fundamental role for thermal stability of active pharmaceutical ingredients and organic glasses in general. Prevention of this detrimental effect might be potentially realized via annealing at the materials' softening point to mend/reduce the quantity of the defects. Alternatively, spray-drying may be used as a superior method for preparation of thermally stable fine-sized particles of certain APIs.

Acknowledgements

This work has been supported by the Czech Science Foundation under project No. 17-11753S, and by the projects LM2015082 a CZ.02.1.01/0.0/0.0/16_013/0001829. The authors also thank to L. Beneš for the XRD measurements and to J. Havlíček for the NMR measurements.

References

- Avrami M., 1939. Kinetics of phase change I—general theory. *J. Chem. Phys.* 7, 1103–12.
- Avrami M., 1940. Kinetics of phase change. II—transformation-time relations for random distribution of nuclei. *J. Chem. Phys.* 7, 212–24.
- Avrami M., 1941. Granulation, phase change, and microstructure – kinetics of phase change III. *J. Chem. Phys.* 7, 177–84.
- Bhattacharya S., Suryanarayanan R., 2009. Local mobility in amorphous pharmaceuticals—characterization and implications on stability. *J. Pharm. Sci.* 98, 2935–53
- Bhugra C., Pikal M.J., 2008. Role of thermodynamic, molecular and kinetic factors in crystallization from the amorphous state. *J. Pharm. Sci.* 97, 1329–49
- Brandová D., Svoboda R., Olmrová Zmrhalová Z., Chovanec J., Bulánek R., 2018. Crystallization kinetics of glassy materials: the ultimate complexity? *J. Therm. Anal. Calorim.* 134, 825-834.
- Chen C.D., Welsbie D.S., Tran C., et al., 2004. Molecular determinants of resistance to antiandrogen-therapy, *Nat. Med.* 10, 33–39.
- Dobrova A., Stoyanov A., Tzuparska S., Gutzow I., 1996. Non-steady-state effects in the kinetics of crystallization of organic polymer glass-forming melts. *Thermochim. Acta* 280-281, 127-151.
- Hancock B.C., Zografi G., 1997. Characteristics and significance of the amorphous state in pharmaceutical systems. *J. Pharm. Sci.* 86, 1–12.

- Janssens S., den Mooter G.V., 2009. Review: physical chemistry of solid dispersions. *J. Pharm. Pharmacol.* 61, 1571–86
- Jemal A., Siegel R., Ward E., et al., 2006. The malignant pleural effusion as a model to investigate intratumoral heterogeneity in lung cancer, *CA Cancer J. Clin.* 56, 106–130.
- Johnson W.A., Mehl K.F., 1939. Reaction kinetics in processes of nucleation and growth. *Trans. Am. Inst. Min. (Metall) Eng.* 135, 416–42.
- Jung M.E., Ouk S., Yoo D., et al., 2010. Structure–activity relationship for thiohydantoin androgen receptor antagonists for castration-resistant prostate cancer (CRPC), *J. Med. Chem.* 53, 2779–2796.
- Kissinger H.E., 1957. Reaction kinetics in differential thermal analysis, *Anal. Chem.* 29, 1702–6.
- Laitinen R., Lobmann K., Strachan C.J., Grohganz H., Rades T., 2013. Emerging trends in the stabilization of amorphous drugs. *Int. J. Pharm.* 453, 65–79.
- Maini L., Braga D., Farinella F., Melotto E., Verzini M., Brescello R., Michieletto I., Munari I., 2018. Crystal forms of Enzalutamide and a crystal engineering route to drug purification. *Cryst. Growth Design* 18, 3774–3780.
- Opfermann J., 2000. Kinetic analysis using multivariate non-linear regression. I. basic concepts. *J. Therm. Anal. Calorim.* 60, 641–658.
- Qin S., Ting C., 2017. Recent progress on crystallization of amorphous pharmaceutical solids. *J. China Pharm. Univ.* 48, 654–662.
- Rams-Baron M., Jachowicz R., Boldyreva E., Zhou D., Jamroz W., Paluch M., 2018. *Amorphous Drugs – Benefits and Challenges*. Springer, e-book ISBN 978-3-319-72002-9.
- Romanová J., Svoboda R., Obadalová I., Beneš L., Pekárek T., Krejčík L., Komersová A., 2018. Amorphous Enzalutamide – non-isothermal recrystallization kinetics and thermal stability. *Thermochim. Acta* 655, 134–141.
- Roseler A., 2015. Xtandi™ (Enzalutamid) now also approved for the Treatment of advanced Prostate Cancer in Chemotherapy-naïve Men. *Oncol. Res. Treat.* 38, 73–73.
- Schittny A., Huwylar J., Puchkov M., 2020. Mechanisms of increased bioavailability through amorphous solid dispersions: a review. *Drug Deliv.* 27, 110–127.
- Šesták J., 1984. *Thermophysical Properties of Solids, Their Measurements and Theoretical Analysis*. Elsevier, Amsterdam.
- Starink M.J., 2003. The determination of activation energy from linear heating rate experiments: a comparison of the accuracy of isoconversion methods, *Thermochim. Acta* 404, 163–76.
- Sun Y., Zhu L., Wu T., Cai T., Gunn E.M., Yu L., 2012. Stability of Amorphous Pharmaceutical Solids: Crystal Growth Mechanisms and Effect of Polymer Additives. *AAPS. J.* 14, 380–388.
- Svoboda R., Brandová D., 2017. Crystal growth from mechanically induced defects: A phenomenon observed for glassy materials. *J. Therm. Anal. Calorim.* 127, 799 - 808.
- Svoboda R., Bulánek R., Galusek D., Hadidimasouleh R., Ganjkanlou Y., 2018. Crystal formation in vanadium-doped zirconia ceramics. *CrystEngComm* 20, 3105–3116.
- Svoboda R., Málek J., 2011. Interpretation of crystallization kinetics results provided by DSC. *Thermochimica Acta* 526, 237–251.
- Svoboda R., Pérez-Maqueda L., Podzemná V., Perejón A., Svoboda O., 2020. Influence of DSC thermal lag on evaluation of crystallization kinetics. *J. Non-Cryst. Sol.* 528, 119738.
- Tool A.Q., 1946. Relation between inelastic deformability and thermal expansion of glass in its annealing range. *J. Am. Ceram. Soc.* 29, 240–253.
- Tran C., Ouk S., Clegg N.J., et al., 2009. Emerging therapeutic approaches in the management of metastatic castration-resistant prostate cancer, *Science* 324, 787–790.

- Tran C, Ouk S, Clegg NJ, et al., 2009. Development of a second-generation antiandrogen for treatment of advanced prostate cancer. *Science* 324, 787–90.
- Trasi N.S., Boerrigter S.X.M., Byrn S.R., 2010. Investigation of the milling-induced thermal behavior of crystalline and amorphous griseofulvin. *Pharm. Res.* 27, 1377-1389.
- Tyrrel C.J., Kaisary A.V., Iversen P., et al., 1998. Treating prostate cancer in elderly men: how does aging affect the outcome, *Eur. Urol.* 33, 447–456.
- Wilson V., Lou X., Osterling D.J., Stolarik D.F., Jenkins G., Gao W., Thang G.G.Z., Taylor L.S., 2018. Relationship between amorphous solid dispersion *in vivo* absorption and *in vitro* dissolution: phase behavior during dissolution, speciation, and membrane mass transport. *J. Control. Release* 292 172-182.
- Yu L., 2001. Amorphous pharmaceutical solids: preparation, characterization and stabilization. *Adv. Drug Deliv. Rev.* 48, 27–42
- Zhou D., Schmitt E.A., Zhang G.G., Law D., Vyazovkin S., Wight C.A., Grant D.J.W., 2003. Crystallization Kinetics of Amorphous Nifedipine Studied by Model-Fitting and Model-Free Approaches. *J. Pharm. Sci.* 92, 1779-1792.



Figure captions

- Fig. 1: Example DSC curves obtained at $10\text{ }^{\circ}\text{C}\cdot\text{min}^{-1}$ for the air-cooled HME (black curves), LN_2 -cooled HME (red curves) and spray-dried (blue curves) Enzalutamide. The particular particle size ranges are indicated.
- Fig. 2: Stacked (graph A) and shifted (graph B) NMR spectra for air-cooled, LN_2 -cooled and spray-dried as-prepared Enzalutamide materials, compared to the signals corresponding to the materials with known degree of crystallinity. Graph C shows the diffraction patterns of as-prepared and DSC-crystallized air-cooled, LN_2 -cooled and spray-dried Enzalutamide materials.
- Fig. 3: A) Cross-section of partially crystallized air-cooled HME-produced 20-50 μm particle. The scale bar indicates 5 μm size.
 B) Fully crystallized air-cooled HME-produced 20-50 μm particle. The scale bar indicates 5 μm size.
 C) Cross-section of partially crystallized LN_2 -cooled HME-produced 20-50 μm particle. The scale bar indicates 5 μm size.
 D) Fully crystallized LN_2 -cooled HME-produced 20-50 μm particle. The scale bar indicates 5 μm size.

- Fig. 4: A) Cross-section of partially crystallized air-cooled HME-produced 300-500 μm particle. The scale bar indicates 20 μm size.
 B) Zoomed-in surface crystalline layer from Fig. 4A. The scale bar indicates 2 μm size.
 C) Cross-section of partially crystallized LN_2 -cooled HME-produced 300-500 μm particle. The scale bar indicates 5 μm size.
 D) Fully crystallized spray-dried Enzalutamide. The scale bar indicates 1 μm size.

Fig. 5: DSC curves obtained for the air-cooled (graphs A, C and E) and LN_2 -cooled (graphs B, D and F) HME-produced Enzalutamide. Arrows and color schemes indicate the direction in which q^+ increases. Exothermic effects evolve in the upwards direction. Graphs A and B show data for the 20 - 50 μm powders; graphs C and D show data for the 50 - 125 μm powders; graphs E and F show data for the 300 - 500 μm powders.

- Fig. 6: A) Crystallization enthalpies evaluated for the HME- and SD-produced Enzalutamide materials plotted in dependence on the averaged particle size. The empty points correspond to ΔH_1 for the first crystallization peak of the 20-50 μm powders; the percent $\Delta H_1/\Delta H$ ratio is shown in label.
 B) Kissinger plot for the studied Enzalutamide amorphous powders.
 C) Activation energies of the crystallization process evaluated by the Starink method for the HME- and SD-produced Enzalutamide materials plotted in dependence on the averaged particle size. In case of the 20-50 μm powders only the data for the first crystallization peak (dominantly responsible for the crystal growth at low temperatures) were taken for the evaluation.

- Fig. 7: A) Prediction of Enzalutamide crystallization behavior at 50 $^\circ\text{C}$ based on the kinetic parameters obtained during the MKA optimizations of the data-curves obtained at 0.5 $^\circ\text{C}\cdot\text{min}^{-1}$.
 B) Data from graph A zoomed-in on the X axis.
 C) Prediction of Enzalutamide crystallization behavior at 100 $^\circ\text{C}$ based on the kinetic parameters obtained during the MKA optimizations of the data-curves obtained at 0.5 $^\circ\text{C}\cdot\text{min}^{-1}$.
 D) Data from graph C zoomed-in on the X axis.
 E) Results of the particle size analysis for the air-cooled HME-produced Enzalutamide (red columns). Theoretical particle size distribution (blue columns) calculated on the basis of the extended non-linear optimization fitting the isothermal annealing data of the unsieved material with the extended kinetic predictions of the d_{aver} fractions investigated in this work (blue line in graph F) – see text for details.
 F) Black line - isothermal crystallization α -t dependence of unsieved air-cooled HME-produced Enzalutamide (details of the experiment and raw DSC data are shown in the inset). Red dashed line – fit of the experiment via the three base kinetic predictions corresponding to the kinetic results of the 20 - 50, 50 - 125 μm and 300 - 500 μm particle size fractions. Blue line – fit of the experiment via the kinetic predictions corresponding to the three experimentally obtained kinetic datasets (for the 20 - 50, 50 - 125 and 300 - 500 μm powder fractions) and three other datasets, theoretically calculated for 125 - 180, 180 - 250 and 250 - 300 μm powders.

Table 1

A) Kinetic parameters determined by the overall MKA applied to the whole set of kinetic data obtained at all applied q^+ .

B) Kinetic parameters determined by the modified single-curve MKA applied to the kinetic data obtained at $0.5\text{ }^{\circ}\text{C}\cdot\text{min}^{-1}$ (these values were used for the kinetic predictions of isothermal crystal growth).

A							
ID	air-cooled HME			LN ₂ -cooled HME			SD
d/ μm	20-50	50-125	300-500	20-50	50-125	300-500	0.1-1
E(kJ/mol)	137.0	143.1	136.1	143.9	146.3	130.6	113.7
log(A/s)	17.21	16.86	15.8	17.76	17.16	14.88	12.89
M	0.02	0.490	0.687	0.112	0.559	0.631	0.243
N	0.258	0.567	0.928	1.031	0.575	0.759	0.724

B							
ID	air-cooled HME			LN ₂ -cooled HME			SD
d/ μm	20-50	50-125	300-500	20-50	50-125	300-500	0.1-1
E(kJ/mol)	163.1	159.8	162.6	144.7	133.2	139.5	187.0
log(A/s)	22.28	19.06	19.26	19.21	15.87	16.13	24.26
M	0.612	0.538	0.757	0.530	0.791	0.701	0.568
N	0.757	0	0	0.797	0	0	1

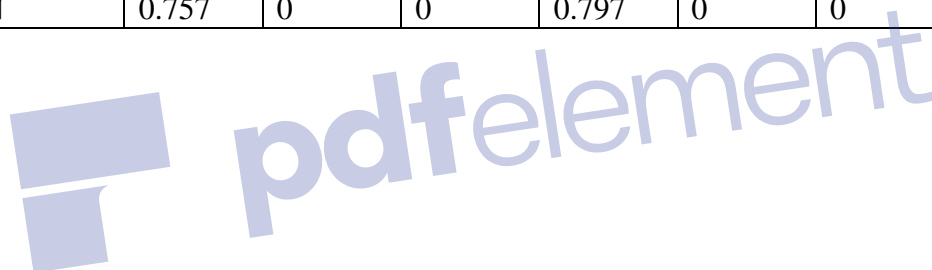


Figure 1

[Click here to download high resolution image](#)

Remove Watermark Now

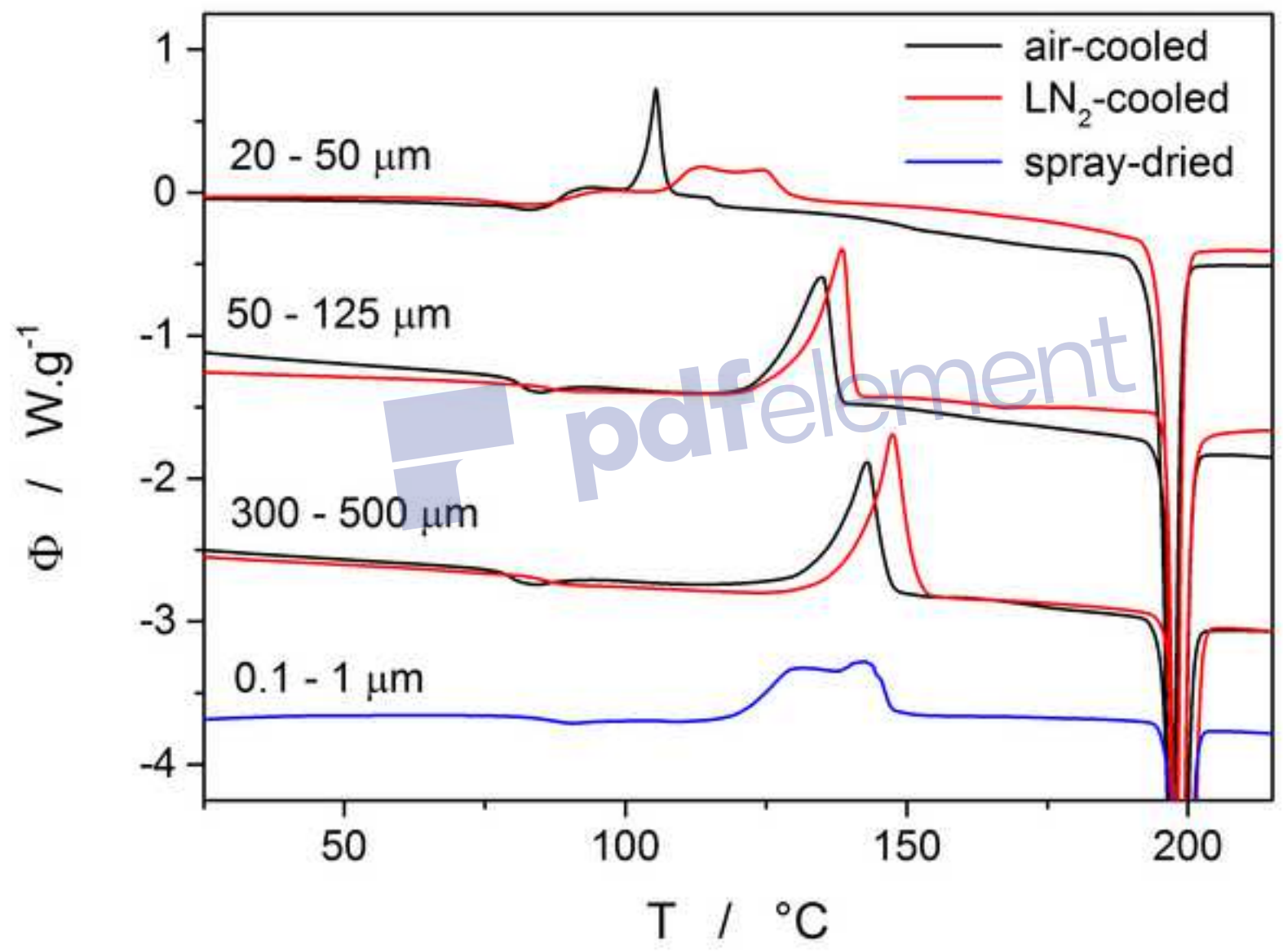


Figure 2
[Click here to download high resolution image](#)

Remove Watermark Now

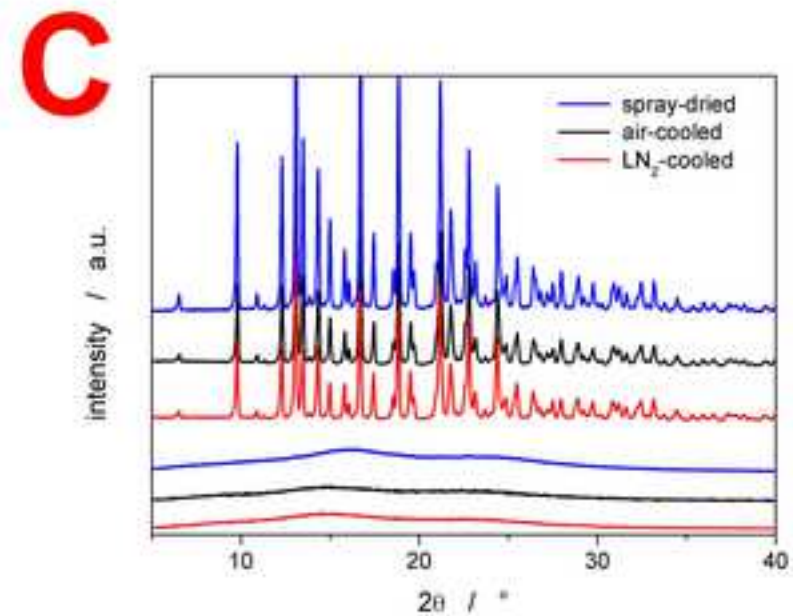
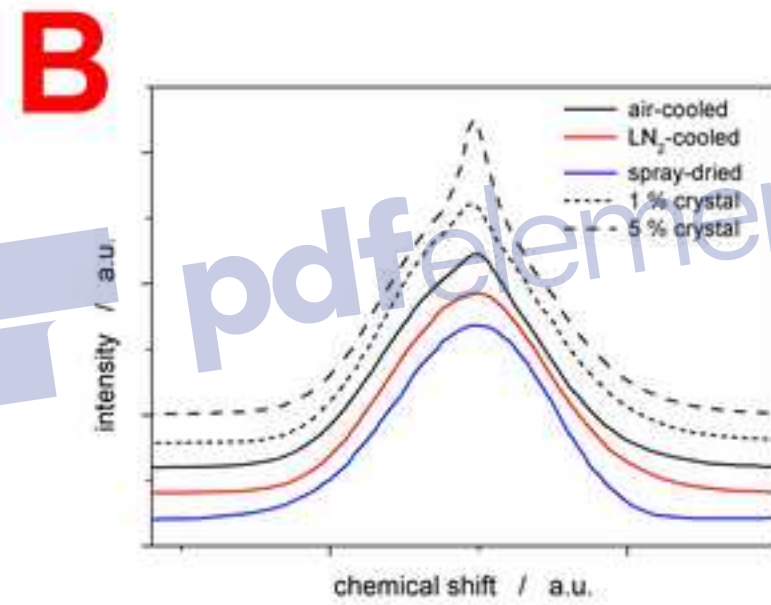
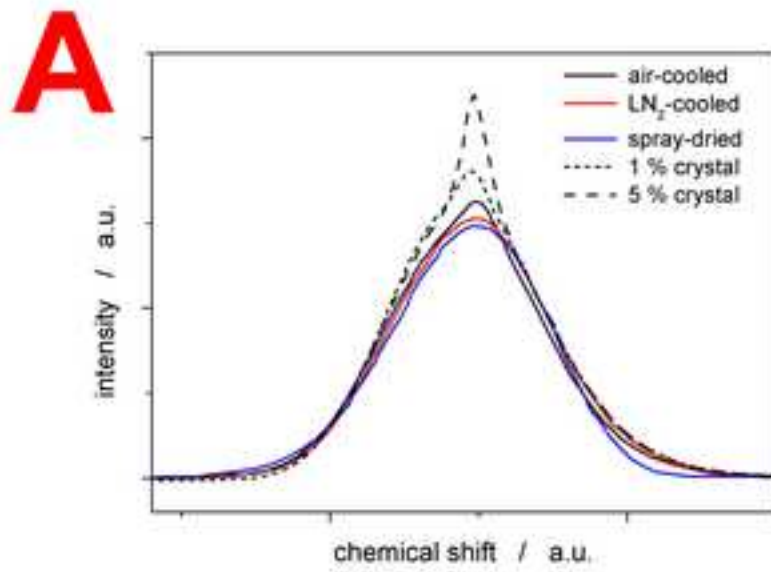


Figure 3
[Click here to download high resolution image](#)

Remove Watermark Now

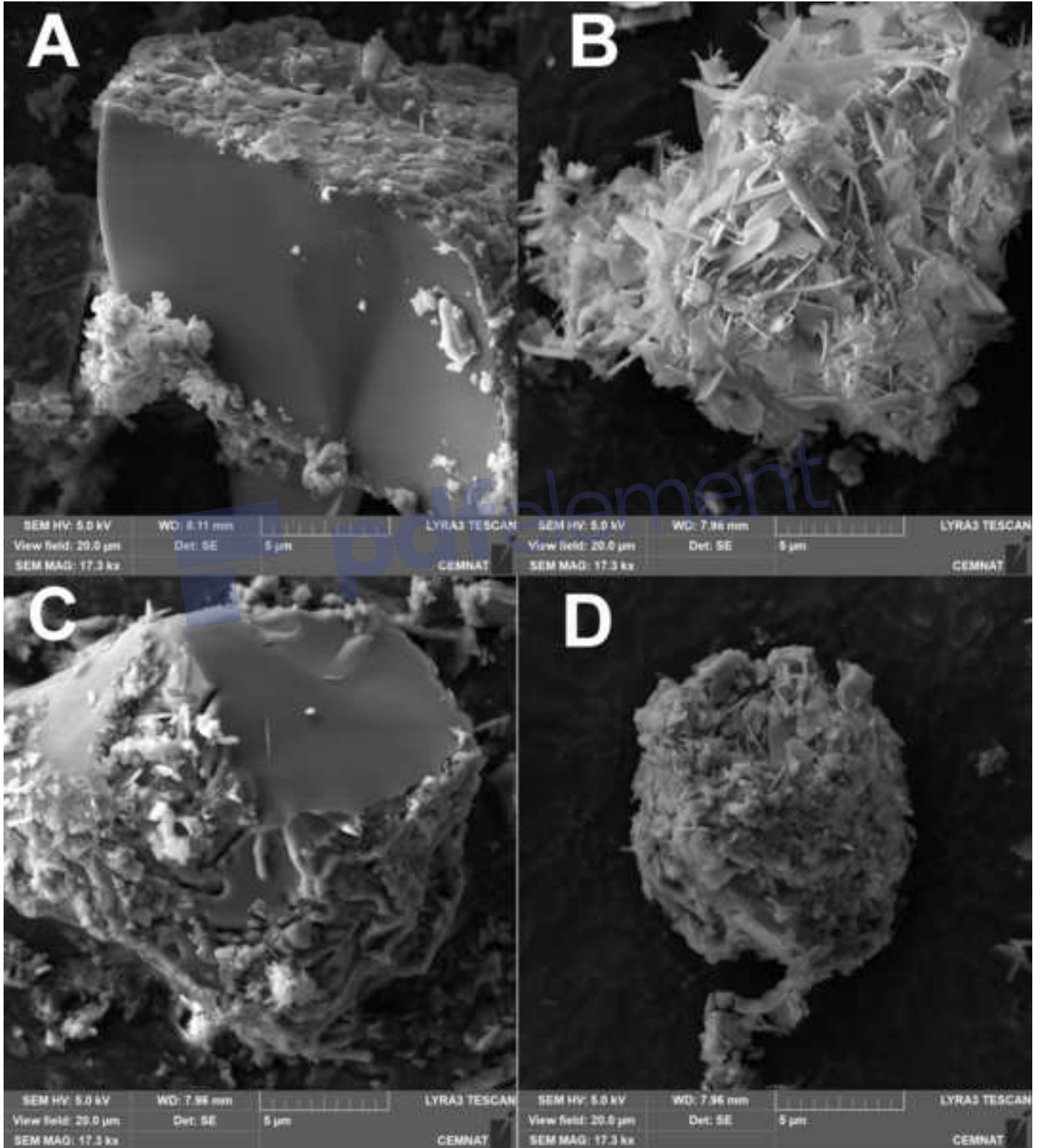


Figure 4
[Click here to download high resolution image](#)

Remove Watermark Now

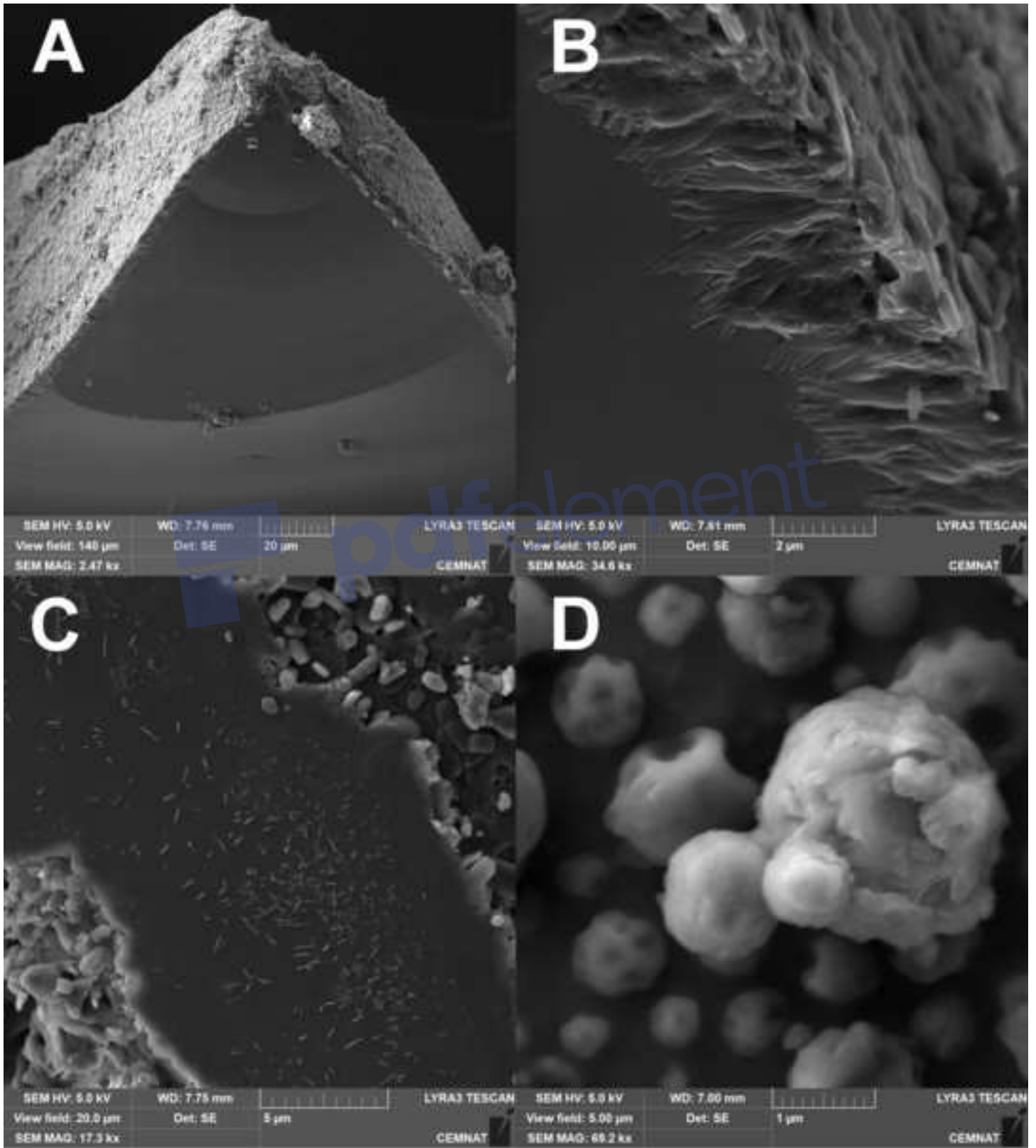


Figure 5

[Click here to download high resolution image](#)

Remove Watermark Now

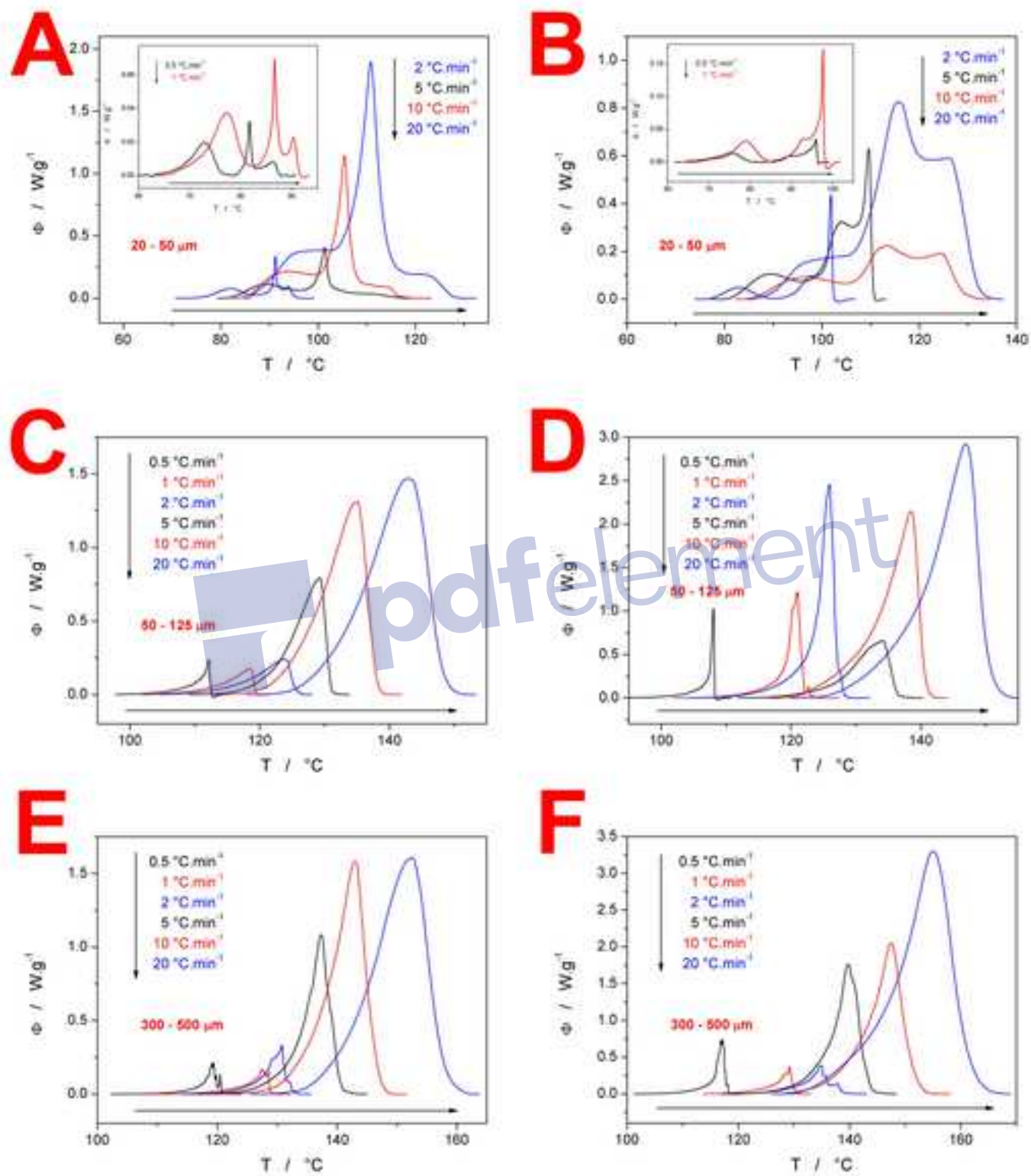


Figure 6
[Click here to download high resolution image](#)

Remove Watermark Now

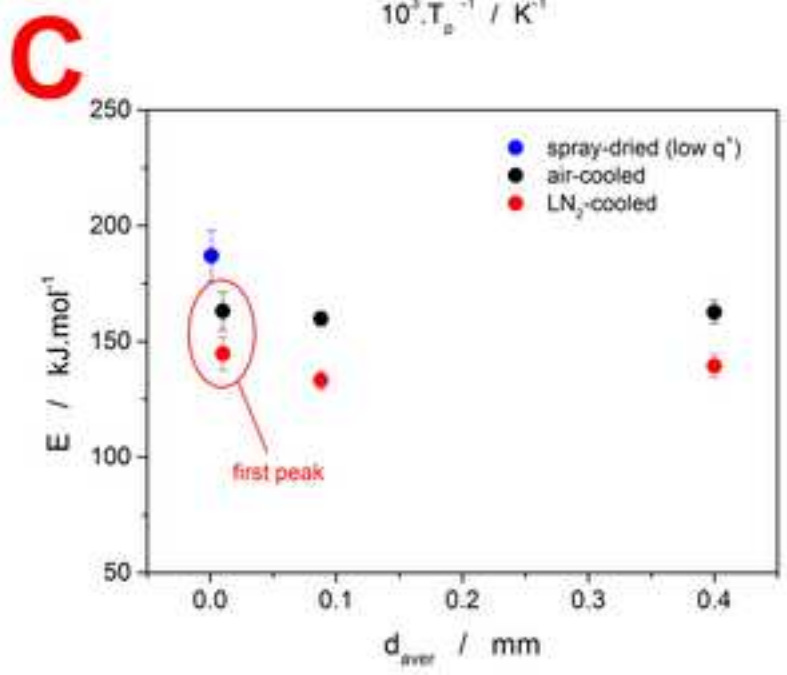
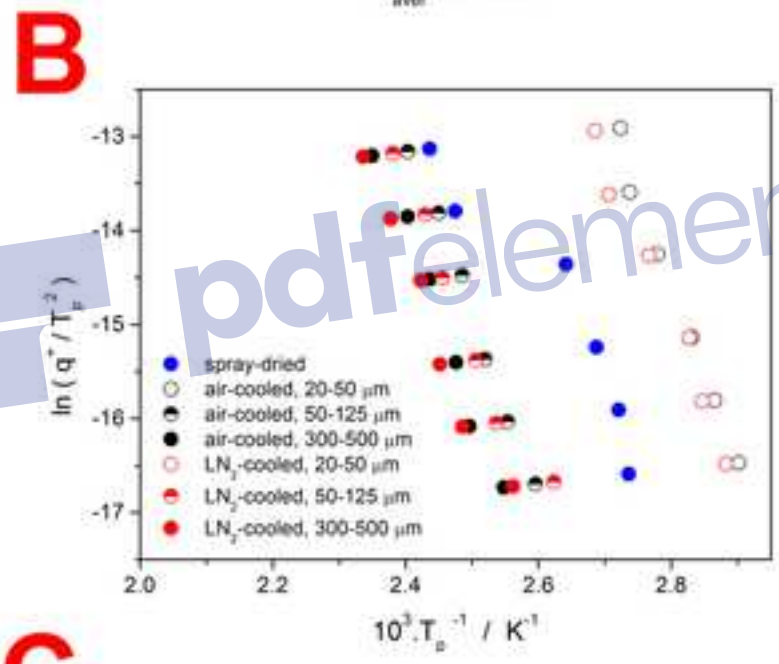
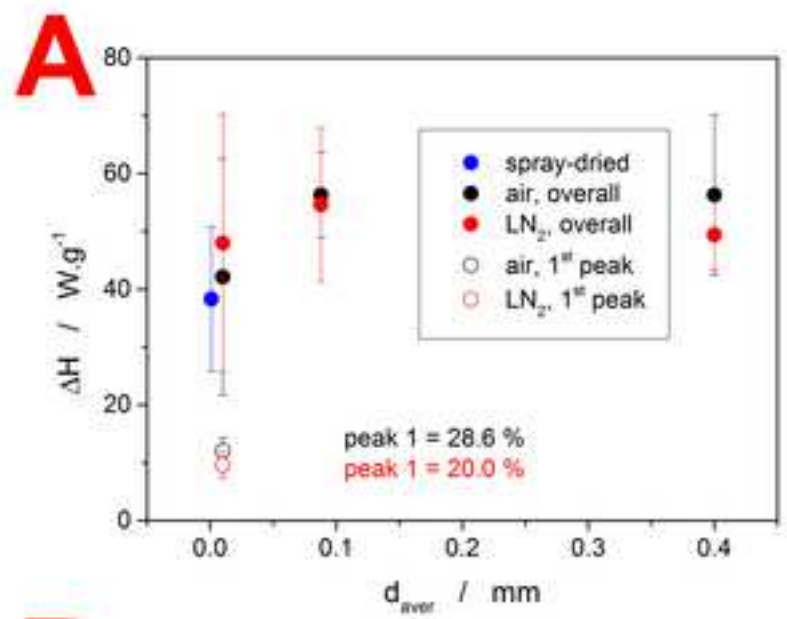


Figure 7
[Click here to download high resolution image](#)

Remove Watermark Now

